Computational Condensed Matter 16 (2018) e00327

Contents lists available at ScienceDirect

Computational Condensed Matter

journal homepage: http://ees.elsevier.com/cocom/default.asp

Structural, electronic and hyperfine properties on Sm_2O_3, Eu_2O_3 and Gd_2O_3 phases

D. Richard [a, *], L.A. Errico [a, b], M. Rentería [a]

[a] Departamento de Física and Instituto de Física La Plata (IFLP, CONICET), Facultad de Ciencias Exactas, Universidad Nacional de La Plata, CC 67, 1900, La Plata, Argentina

[b] Universidad Nacional del Noroeste de la Pcia. de Buenos Aires (UNNOBA), Monteagudo, 2772, 2700, Pergamino, Argentina

ARTICLE INFO

Article history:
Received 4 June 2018
Received in revised form
9 August 2018
Accepted 11 August 2018

Keywords:
Lanthanide oxide
Mechanical properties
Hyperfine interactions
Electric-field-gradient
DFT calculations

ABSTRACT

We present a detailed first-principles study of three rare-earth lanthanide sesquioxides (Ln_2O_3, Ln = Sm, Eu, and Gd) in the hexagonal A, the monoclinic B, and the cubic C phases. The calculations were performed with the Density Functional Theory (DFT)-based Augmented Plane Wave plus local orbital (APW + lo) method, using the local spin density approximation (LSDA) and the LSDA + *U* approach to take into account the strongly correlated Ln-4*f* electrons. We calculated the equilibrium structures and the effect of hydrostatic pressure on them, the density of states (DOS), the energy band-gaps and, finally, the electric-field-gradient (EFG) tensor at the different cationic sites. The obtained predictions reveal that for the three considered Ln_2O_3 sesquioxides, the C phase is the stable one, with a transition pressure to the A phase of about 1−2 GPa.

For each Ln_2O_3, the predicted properties were compared with those obtained by means of different experimental techniques. We found that the crystal equilibrium volume, bulk modulus and its first pressure derivative obtained with LSDA are in good agreement with previous experimental results. On the other hand, the inclusion of the *U* term gives a correct description of the insulating ground state of these systems. Concerning the EFG tensor, LSDA and LSDA + *U* predict similar values for the EFG at each cationic site in all cases. These results are consistent with the hyperfine interactions experiments reported for the B and C phases of Gd_2O_3. Finally, we analyze the origin of the EFG at Ln sites, by considering the contributions of the different Ln orbitals to it, and its relation with the local structure.

1. Introduction

The lanthanide sesquioxides (Ln_2O_3) have been extensively studied due to their broad technological significance, and many review articles describing their crystallographic forms and thermodynamics have appeared [1–3]. These compounds are known to occur in five distinct polymorphic modifications. In temperatures below 2000 °C, these oxides exist in three crystal systems: the hexagonal phase (A-type, space group P-3m1), the monoclinic phase (B-type, C2/m), and the cubic phase (C-type, Ia-3). At higher temperatures, the phases designated as H and X are formed [1]. Regarding the lanthanide sesquioxides in the middle of the Ln series (Sm_2O_3, Eu_2O_3 and Gd_2O_3), they are stable in either the B or C phase under ambient conditions and, with increasing temperature, the phase transformation sequence is generalized by the order C→B→A. On the other hand, by applying pressure, these oxides prefer to form the A phase rather than the B and C ones, and the B phase than the C one [1].

In the last years, new experimental investigations went deeper into the analysis of Ln_2O_3 phase transitions showing that the current available data of all Ln_2O_3 polymorphs in the literature are still insufficient. For example, McClure reported a novel pressure induced A-type phase for La_2O_3 [4], and Atkinson studied in detail monoclinic Gd_2O_3 and found a temperature-induced method to obtain this phase [5]. So, the construction of Ln_2O_3 phase diagrams and the study of the involved structures and their related properties are still ongoing [3,6].

This experimental background is complemented with first principles studies. In this respect, several Density Functional Theory (DFT) methods were applied to analyze Ln_2O_3 oxides [7–11]. These compounds are particularly challenging due to the presence of Ln-4*f* electrons, which have strong electronic correlation effects

* Corresponding author.
E-mail address: richard@fisica.unlp.edu.ar (D. Richard).

https://doi.org/10.1016/j.cocom.2018.e00327
2352-2143/

that difficult an adequate *ab initio* description by only considering the standard DFT. Although different approaches have been used to deal with the Ln_2O_3 structures, the most common is the Projector Augmented Wave (PAW) method. In this respect, the equilibrium structures were systematically studied for the Ln_2O_3 series considering the oxides phases by pairs (*i.e.*, A- and B-, or A- and C-phases were studied together in a same paper) [7–10]. Regarding the middle oxides, there exist some PAW studies that consider these compounds separately, and analyze their structural properties and phase transitions [12–14]. So, there is not a comparative study for the three phases in Sm_2O_3, Eu_2O_3, and Gd_2O_3. Also, previous PAW studies did not deal with the strongly correlated Ln-4*f* electrons because they treated these orbitals as core states, which is essentially equivalent to treat them as filled atomic-like 4*f* levels [10,15,16]. In order to improve the description of these systems, alternative *ab initio* strategies have been implemented: those that improve the PAW potentials [17,18], explicitly account for the self-interaction [8,11], or made use of hybrid functionals [19]. But these alternatives suffer from extremely demanding computational costs, or from the controversy behind how to proceed with the inclusion of "corrections" to a first principles method.

Currently, methods that include a Hubbard term (DFT + *U*) have emerged to improve the predicted properties of Ln compounds compared to standard DFT, without an additional computational cost [20–24]. In these cases, the inclusion of *U* terms means the addition of arbitrary parameters and opens new questions on the predicted physics of the modeled compounds that continuously request experimental verification [25]. Recently, we started studies on Ln_2O_3 systems considering the Augmented Plane Waves plus local orbitals (APW + lo) approach with the addition of a Hubbard term. We systematically analyzed the predicted equilibrium structures of Ln_2O_3 with the A and C phases [26]. Our earlier experience has shown that such all-electron method gives an adequate description of the structural and electronic properties of the pure compounds, and in many cases it can successfully predict the electric field gradient (EFG) at the atomic sites of the structure [22,26–28]. The EFG tensor is a quantity extremely sensitive to small changes in the asymmetry of the electronic charge density close to the considered atomic site (due to its r^{-3} dependence from the charge sources). So, this hyperfine property is a very suited tool for investigating the structural environment at a subnanoscopic scale in each phase, and for testing the theoretical modeling from another point of view.

In this work, we present detailed DFT + *U* calculations of the structural, electronic, and hyperfine properties of Sm_2O_3, Eu_2O_3, and Gd_2O_3 in their A, B and C phases. These calculations were performed with the APW + lo method, using the local spin density approximation (LSDA), and also including the Hubbard *U* term (LSDA + *U* approach) to take into account the strongly correlated Ln-4*f* electrons. The aim of the present study is to gather more information about strengths and weaknesses of the DFT + *U* approach on predicting such variety of properties. To our knowledge, this is the first time that these properties are simultaneously analyzed by first principles in the monoclinic phase, and compared with those of the other two phases.

The organization of this paper is as follows: in Section 2 we introduce the crystal structure of the considered polymorphs of Ln_2O_3. In Section 3 we describe our method of calculation, and in Section 4 we present and discuss our results. Finally, in Section 5 the conclusions are drawn.

2. Lanthanide sesquioxide structures

The hexagonal A-Ln_2O_3 structure has a lattice parameter ratio *c*/*a* near to 1.55. The unit cell contains one formula unit, with two symmetry-equivalent Ln atoms (called LnA in the following) and two types of oxygen atoms (O1 and O2). The two LnA atoms are located at the positions ±(1/3, 2/3, *u*), two O2 atoms are at ±(1/3, 2/3, *v*), and the O1 atom is at the origin of the unit cell (see Fig. 1a) [29]. Hence, all the atomic positions for the A-type unit cell are determined by two internal parameters (*u* and *v*). The O1 and O2 atoms have different Ln coordination: the O1 atom is surrounded by six LnA atoms, while the O2 atoms are found in the center of a tetrahedron of four LnA atoms. The LnA atoms are coordinated with seven nearest oxygen neighbors (ONNs, see Fig. 1b).

The B-Ln_2O_3 structure is less compact than that corresponding to the A phase, and corresponds to a monoclinic distortion of the A phase, with six formula unit per unit cell (Fig. 2a). There are three inequivalent Ln sites (called LnB1, LnB2, and LnB3 in what follows), which are equally abundant in the structure, and are all seven-fold coordinated. However, for the LnB3 atom the seventh ONN is sufficiently far and is commonly considered as six-fold coordinated [1,29] (see Fig. 2b–d). On the other hand, the O atoms are coordinated by 4–6 Ln atoms, depending on the considered oxygen. The internal coordinates of Ln and O atoms in the B phase depend on a set of fourteen internal parameters, reported in the literature [29].

Finally, the unit cell of the cubic C-type structure contains sixteen Ln_2O_3 formula units (Fig. 3a). It has two inequivalent crystallographic sites for Ln atoms (LnC1 and LnC2), and one site for the oxygen atoms. The positions of all the atoms in the C-type unit cell are determined by four internal parameters which determine the positions of the LnC1 and O atoms [29]. All oxygen sites are coordinated by four Ln atoms, while the LnC1 and LnC2 sites are both coordinated with six ONNs (see Fig. 3b and d). LnC2 site is axially symmetric, while LnC1 is not. The relative abundance of these cationic sites in the lattice is $f_{C1}/f_{C2} = 3$ [29].

The three phases considered are such that the Ln_2O_3 density monotonically increases with the C→B→A transformations. This is consistent with the progressive change of cation surroundings during the transformations: while C and A-type structures have a single type of ONN coordination polyhedron, with LnO_6 in the cubic C-type and LnO_7 in the A-type, the B-type structure can be considered having a mixture of both polyhedra.

These structures and the transition pressures have been recently experimentally investigated to some extent, either by X-ray diffraction (XRD) [4–6,12–14,30–35], neutron diffraction [36], and other experimental techniques such as energy-dispersive XRD [37] or Raman spectroscopy [38]. In addition, in some cases hyperfine interactions techniques allowed the study of the EFG tensor at Ln sites [39–41]. As we mentioned earlier, the EFG tensor is extremely sensitive to small changes in the asymmetry of the charge density surrounding a given probe-nucleus. This magnitude is a rank 2 traceless symmetric tensor whose components V_{ij} are defined by the second derivative of the Coulomb potential $V(\mathbf{r})$ with respect to

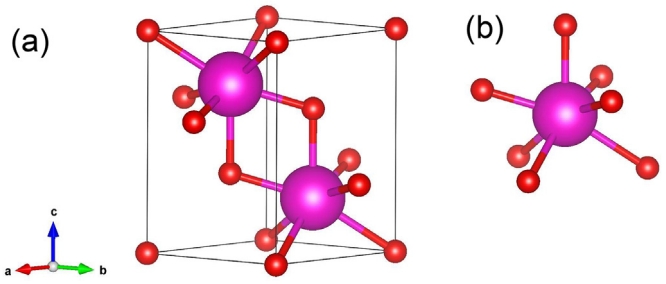

Fig. 1. (a) A-type Ln_2O_3 unit cell and (b) the nearest neighbor coordination for the LnA site of the structure. The large spheres stand for Ln atoms, while the small ones represent oxygen atoms.

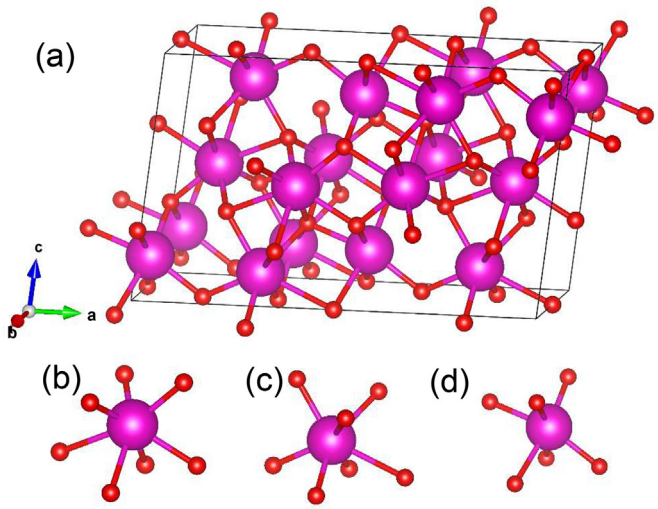

Fig. 2. (a) B-type Ln_2O_3 unit cell and the nearest neighbor coordination for sites (b) LnB1, (c) LnB2, and (d) LnB3.

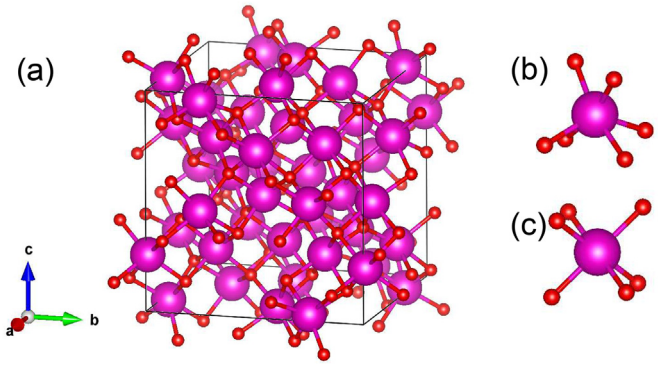

Fig. 3. (a) C-type Ln_2O_3 unit cell and the nearest neighbor coordination for sites (b) LnC1 and (c) LnC2.

the spatial coordinates. In the principal axis system the three diagonal components of the EFG tensor are labeled according to the conventional choice $|V_{xx}|<|V_{yy}|<|V_{zz}|$. The EFG is frequently characterized by its largest eigenvalue V_{zz} and the asymmetry parameter $\eta = (V_{xx}\text{-}V_{yy})/V_{zz}$. By using Mössbauer spectroscopy the quadrupole splitting (ΔE_Q) can be measured, which for the $I = 3/2$ state of the ^{155}Gd probe is related to V_{zz} and η by:

$$\Delta E_Q = \frac{eQ}{2} V_{zz}\left(1+\frac{\eta^2}{3}\right)^{\frac{1}{2}} \quad (1)$$

where Q is the nuclear quadrupole moment of the ^{155}Gd sensitive state.

3. Calculation details

We performed spin-polarized *ab initio* electronic structure calculations with the WIEN2k implementation of the APW + lo method [42]. The exchange and correlation potential was treated using both the LSDA approximation [43] and the LSDA + U approach in the self-interaction-corrected scheme [44,45]. In the last case, considering our previous investigations [22,26,28], we took $U = 10.9$ eV (0.8 Ry) for Ln-4*f* orbitals. This choice has already shown a good description of the electronic density of states (DOS) in Ln_2O_3 systems. The muffin-tin radii (R_{MT}) used for the Ln and O atoms were 1.16 and 0.93 Å, respectively. The wavefunctions in the interstitial region were expanded in planewaves using a cutoff parameter $R_{MT}K_{max} = 9$, where K_{max} is the maximum modulus for the reciprocal lattice vector and R_{MT} considered for this parameter stands for the smallest atomic muffin-tin sphere radius. Integration in the reciprocal space was performed using the tetrahedron method, taking up to 100 *k*-points in the first Brillouin zone, and we used a largest vector in the charge density Fourier expansion of $G_{max} = 12/a_0$ (being a_0 the Bohr radius). In each case, the self-consistent calculation was achieved by considering a total energy tolerance of 0.1 mRy. Once self-consistency of the potential was achieved, we determined the equilibrium atomic internal coordinates according to a Newton-damped scheme of the quantum-mechanically-derived forces acting on the atoms to within a force tolerance of 0.025 eV/Å.

For all the considered phases, the total energies E were calculated self-consistently for different values of the unit cell volume around the equilibrium value V_0. In this respect, the chosen R_{MT} allowed the calculation of E up to a volume compression of about 10% with respect to V_0. The Birch-Murnaghan equation of state (EOS) was fitted to the obtained $E(V)$ data to determine the equilibrium structural properties of each compound [46,47]. In the case of Ln_2O_3 systems with the non-cubic A and B phases, the calculation of equilibrium structures required additional calculations over all the degrees of freedom in each structure (*i.e.*, the c/a ratio in the case of the A phase, and the three lattice parameters and β angle for the B phase).

Once we obtained the equilibrium structures, we predicted the structural phase stability by estimating the transition enthalpies ΔH and transition pressures p_{tran} between phases from the $E(V)$ curves [9]. On the other hand, we calculated the DOS, from which we determined the energy band-gap E_g in each case. Finally, we predicted the diagonal elements of the EFG tensor at the different atomic sites from the V_{2M} harmonic coefficients of the potential [48].

We have to remark that in a previous study we explored the structures of Ln_2O_3 systems in the A and C phases [26], and in that case for the A phase we fixed the c/a ratio at the experimental value. Also, in another study we analyzed the EFG in C-type Ln_2O_3 systems, but fixing the unit cell volume at the experimental value [22]. In the present work we analyze for the first time the equilibrium structures of the middle Ln_2O_3 systems in the A, B, and C phases, and we relate them with the EFGs at the Ln sites. So, in all these cases we will explore the structures without recurring to experimental constrains, and we will include the monoclinic B phase for the first time in a study of this kind.

4. Results and discussion

4.1. Structural properties

In Fig. 4 we present the $E(V)$ curves corresponding to the A, B, and C phases of Eu_2O_3 calculated with the LSDA approximation. The solid lines stand for the fits of the Birch-Murnaghan EOS to the $E(V)$ data, from which we determine the equilibrium volume V_0, the bulk modulus B and its derivative with respect to pressure B'. The obtained structural parameters for each Ln_2O_3 system are presented in Table 1. As mentioned before, in the case of the A phase we also determined the value of the lattice parameter c which optimizes the hexagonal structure from the calculation of E as a function of c/a ratio. Also, in a more complex way, for the B phase we determined the three lattice parameters and the β angle that optimize the unit cell from multiple optimization steps. All these parameters calculated with LSDA are presented in Table 1, where we also included

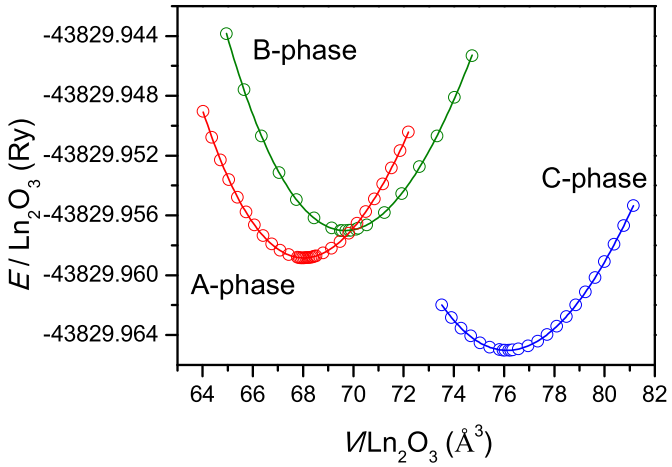

Fig. 4. $E(V)$ curves for Eu_2O_3 obtained using the LSDA approximation. The solid lines correspond to Birch-Murnaghan EOS fits.

recent experimental room temperature measurements presented by other authors. By including experimental results our aim was to show the range of experimental values reported in the literature in the last years for these sesquioxides, in order to perform an overall comparison between predicted and measured values. A detailed description of the origin of those experimental results is provided as supplementary material. On the other hand, the structural results we obtained with the LSDA + U approach are provided also as supplementary material (we must say in advance that it gave similar results to LSDA). As can be seen in Table 1, we predict for the hexagonal A phase a c/a ratio that ranges from 1.53 to 1.57, while for the B phase we found β in the order of 100° for the three oxides.

Regarding V_0, we found for the three phases that it slightly decreases with Ln atomic number (Z_{Ln}), in agreement with the so-called lanthanide contraction [1]. On the other hand, for a given Ln_2O_3 system, the A-type structure has an equilibrium volume about 2% smaller than that of the B-type structure, and the value of V_0 for the B phase is about 9% smaller than that of the C one (see Table 1). The inclusion of the U term increases V_0 in about 2% compared to LSDA, being the LSDA + U predictions for V_0 about 4% below the experimental volume (see supplementary material). Hence, our results follow the general trend for Ln_2O_3 polymorphs experimentally observed and, considering the well known tendency of LSDA to underestimate the volume cell [26,49], our predictions for the lattice parameters for each phase are in a good agreement with the experimental values.

Regarding the bulk modulus, for the three phases our predicted values increase with Z_{Ln} in about 10% from Sm_2O_3 to Gd_2O_3. Also, for each system the A-type structure has the highest B value, being about 2% higher than that of the B phase, and 10% higher than the one of the C phase. This result is in agreement with the fact that the A phase has the most compact structure among the three considered, as mentioned before.

Finally, we found that the bulk modulus pressure derivative B' ranges between 3 and 5. Considering the dispersion of the available experimental data for B and B' (that in many cases demands to fix this last value during the fitting procedure), we think that our first principles predictions could help to stablish a more clear distinction between phases through their structural parameters. In particular, we hope that our results could serve as a guide to find an easy way to identify the B phase of these oxides in the laboratory.

4.2. Phase transitions

As can be seen from the $E(V)$ curves corresponding to the Eu_2O_3 example presented in Fig. 4, the most stable phase for this compound is the C one, followed by the A phase, while the B phase has the highest lattice energy. Similar results were obtained for Sm_2O_3 and Gd_2O_3. In order to quantify the phase stability and to study the phase transitions, we estimated the transition enthalpies ΔH from one phase to another at $p = 0$, *i.e.*, between equilibrium volumes. In those cases, ΔH becomes equal to ΔE_0 (being E_0 the energy per formula unit at V_0 obtained from the fit of Birch-Murnaghan EOS to $E(V)$ data). For each compound we also determined the transition pressures p_{tran} between phases by calculating the common tangent slope to pairs of fitted $E(V)$ curves [9]. The obtained LSDA results are presented in Table 2. We did not present LSDA + U predictions for ΔH and p_{tran} due to the strong sensitivity of H to the U value, as we already demonstrated in a previous study [26]. However, we found that the inclusion of the U term maintains the preference for the C phase for the three compounds considered.

According to our results, for the three considered compounds the most stable C-phase is about 0.05 eV below the A-phase (see Table 2). This energy difference equals to about 4.8 kJ/mol (or 580 K), while that of the C→B transition is about 9.6 kJ/mol (or

Table 1
Predicted equilibrium structures for the A, B and C phases of each studied Ln_2O_3 system using LSDA approximation. Lattice parameters are expressed in Å, β in degrees, V_0 in Å^3, and B in GPa. The listed experimental results for each phase have been taken from the indicated references. The experimental V_0 per formula unit correspond to a room temperature measurement, and the values indicated with an asterisk were kept fixed during the fitting procedure to experimental data.

Phase	Parameter	LSDA (this work)			Experimental			
		Sm_2O_3	Eu_2O_3	Gd_2O_3	Sm_2O_3	Eu_2O_3	Gd_2O_3	Refs.
A	a	3.7024	3.6999	3.6752	3.743–3.756	3.725–3.742	3.67–3.741	4-6,13,14,30-37
	c	5.7376	5.7453	5.7355	5.696–5.901	5.706–5.831	5.597–5.709	
	V_0/Ln_2O_3	68.04	68.02	67.26	69.1–72.1	68.6–70.7	65.3–69.2	
	B	164	161	176	128-224 (23)	134(1)-165(6)	142(14)-174(11)	
	B'	4.55	4.91	3.97	1.5(7)-6.9(1)	4*-4.1 (1)	4*-6 (4)	
B	a	13.9533	13.8463	13.8430	14.168–14.1838	13.8224–14.110	14.032–14.0980	
	b	3.5426	3.5463	3.5149	3.624–3.645	3.602–3.6935	3.5750–3.583	
	c	8.6435	8.6653	8.6223	8.830–8.8577	8.7117–8.808	8.742–8.767	
	β	99.07	99.78	99.76	100.027–100.09	99.28–100.13	100.08–100.13	
	V_0/Ln_2O_3	69.83	69.68	68.79	74.4–75.1	71.2–75.5	72.0–72.7	
	B	157	158	171	153 (7)	139-159 (9)	147 (3)	
	B'	3.07	4.26	4.40	4*	4*-5.1 (1)	4*	
C	a	10.6817	10.6793	10.6340	10.928–10.940	10.851–10.860	10.7193–10.843	
	V_0/Ln_2O_3	76.17	76.12	75.16	81.6–81.8	79.9–80.0	77.0–79.7	
	B	143	143	158	116(1)-149(2)	115(1)-145(2)	118 (20)-188	
	B'	4.12	4.71	4.46	4*	4*-5.9 (4)	4*-14 (8)	

Table 2
LSDA transition enthalpies ΔH (in units of eV per Ln_2O_3 formula unit) and transition pressures p_{tran} (in GPa). The experimental p_{tran} results correspond to room temperature measurements.

	LSDA (this work)						Experimental					
	ΔH			p_{tran}			ΔH		p_{tran}			Refs.
	C→B	B→A	C→A	C→B	B→A	C→A	C→B	B→A	C→B	B→A	C→A	
Sm_2O_3	+0.116	−0.065	+0.051	+3.0	−5.6	+1.0	0.03−0.10	0.02−0.05	9.9	2.5−4.7	4.0−7.5	3,6,13,14,32−35,37,38
Eu_2O_3	+0.109	−0.024	+0.085	+2.7	−2.4	+1.6	0.02−0.18	0.03−0.04	~2	4.3−4.7	4.7−6.0	
Gd_2O_3	+0.085	−0.038	+0.047	+2.2	−3.9	+1.0	0.05−0.09	0.05−0.08	4.87		7.0−12.6	

1160 K). Following this stability preference, the predicted C→B transition pressures double the C→A ones (2.2−3.0 and 1.0−1.6 GPa, respectively). Our main difference with the experiments appears to be the phase transformation sequence: while our 0 K calculations predict a preference for the C→A transition, the experimental phase transformation sequence with temperature is in the order C→B→A [1,3]. Taking into account that our calculations must be considered as a theoretical prediction corresponding to the ground state, further first-principles calculations with an extended DFT method at finite temperatures are needed to a better comparison with experiments (see for example Refs. [50,51]).

On the other hand, regarding the phase transformations with pressure, Zhang et al. reviewed most of the experimental determinations. In this sense, the C→B room temperature transition pressure is between 2 and 4 GPa [3]. Also, there is experimental evidence that supports our predictions of a direct C→A transition with pressure. McClure has reported that for Sm_2O_3, Eu_2O_3 and Gd_2O_3 it starts at 4.3, 6.0 and 7.0 GPa, respectively [4]. Additionally, there are works that report a coexistence of the A and B phases for Sm_2O_3 [13,34] and Gd_2O_3 [14] at similar pressures. On the other hand, it also has been reported a direct shock induced C→A transition in the case of Gd_2O_3 [52], being the transition pressure 4 GPa. In Table 2 we have included the corresponding experimental results to better comparison. As can be seen, and considering the above concerns, our calculations are in a general fair agreement with the available experimental data.

4.3. Density of states and electron density

The electronic DOS predicted by LSDA and LSDA + U for the systems with the B-type structure are presented in Fig. 5. For each Ln_2O_3 oxide, we found that the DOS for the A- and C- phases are quite similar to those presented in this figure. When we consider the LSDA approximation (Fig. 5a), the DOS for Sm_2O_3 and Eu_2O_3 consist of a broad band about 2 eV below the Fermi energy (E_F) which is due to O-2p states, followed (with increasing energy) by a partially filled Ln-4f narrow band at E_F. Later, about 3 eV above E_F, lie the Ln-5d empty states. The difference between the DOS for different Ln atoms is that the Ln-4f band is gradually filled and shifted to lower energies as the number of f electrons increases. For Gd_2O_3, where the Ln cation has the $4f^7$ configuration, the 4f-up band is completely filled, and the 4f-down band is completely empty, in agreement with Hund's first rule. So, the partially filled f band observed in Sm_2O_3 and Eu_2O_3 leads to a metallic ground state in these systems, in agreement with previous LSDA predictions [15,22], but in strong disagreement with the insulator character of these compounds. When the U correction is applied, the empty part of the f band is shifted to higher energies, and lie at the conduction band bottom, and the filled part is pulled down below, being these two sub-bands now separated by $U = 0.8$ R y (see Fig. 5b). The obtained DOS correspond to insulators, being now possible to distinguish a valence band with a predominantly O-2p character separated by about 4 eV from the conduction band with Ln-5d character. So, the LSDA + U calculations predict a forbidden band gap of about 4 eV, while the experimental value ranges between 4.0 and 5.45 eV [53].

In Fig. 6 we present projections of the spin-up electron density $\rho(\boldsymbol{r})$ for the A, B, and C phases of Eu_2O_3, obtained by LSDA and LSDA + U. For each phase, we chose a plane that includes all the different Ln atoms involved with some of their ONN. In this sense, we present $\rho(\boldsymbol{r})$ projections over the (110) plane for the A and C phases, and over the (010) plane for the B phase. As can be seen in Fig. 6, for the three considered phases an extremely small degree of covalence between cations and O atoms exist, independently of the use or not of the Hubbard term. This result is in agreement with the low hybridization between atomic orbitals already indicated in the DOS of Fig. 5, which reflects the predominantly ionic nature of these compounds. On the other hand, the inclusion of the U parameter produces a slight change on the distribution of the 4f states (see Fig. 6), in a way that the total $\rho(\boldsymbol{r})$ around the cation adopts a more pronounced atomic-like character for its 4f orbital.

4.4. Electric-field gradient

In Table 3 we present the results for the EFG at the cationic sites of the three considered Ln_2O_3 compounds in the A, B, and C phases. These results correspond to the equilibrium structures predicted by LSDA and LSDA + U. As can be seen in Table 3, for each phase, for a same Ln site LSDA predicts similar values of V_{zz} and η. However, we observe a slight increase of the V_{zz} magnitude as Ln goes from Sm to Gd, in agreement with the small lanthanide contraction effect for these three atoms that lie in the middle of the Ln series. This result reflects that the additional electron in the Ln muffin-tin sphere when the cation changes from Sm to Eu, and from Eu to Gd, does not have a significant effect on the EFG, suggesting that these electrons are nearly spherical. When we apply the Hubbard correction, we found changes in the predicted V_{zz} below 5%, with exceptions for some Ln sites in Sm_2O_3 and Eu_2O_3, where the change can reach 10%. On the other hand, a different behavior is registered for the case of the EFG at the LnB1 site of Sm_2O_3 and Eu_2O_3, where V_{zz} changes its sign and magnitude when we apply the U term. This is due to a rearrangement of the V_{ii} components that flips the V_{zz} direction, as can also be deduced from the change on η (a high asymmetry parameter means that $|V_{zz}| \sim |V_{yy}|$). Considering that for these LnB1 sites the EFG calculated by LSDA is characterized by a high asymmetry parameter and a small magnitude of $|V_{zz}|$ (below 4×10^{21} V/m^2), then the Hubbard correction produces modifications in the EFG components in such a way that the V_{zz} direction turns to that of V_{yy} determined before with LSDA, because of the mentioned rearrangement of V_{ii} components (we will analyze V_{zz} directions later). Regarding the EFGs at the cationic sites of Gd_2O_3, we observe that the inclusion of the U term does not change significantly the magnitude of the predicted V_{zz} in any Gd site, nor the value of η. This is a consequence of the negligible contribution of the 4f electrons to the total EFG in this case, in agreement with the spherically symmetric half-filled Gd-4f shell.

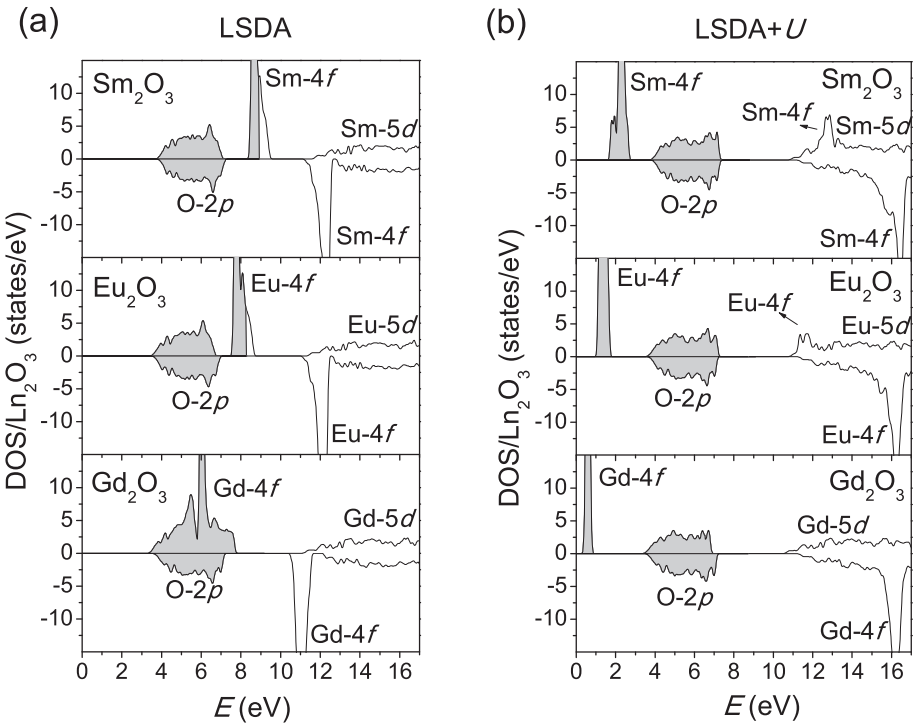

Fig. 5. Calculated total spin-resolved DOS by (a) LSDA and (b) LSDA + U for the B-phases of Ln_2O_3 systems. Shaded areas indicate occupied energy states. In each case, the Fermi level (E_F) is at the end of the shaded area.

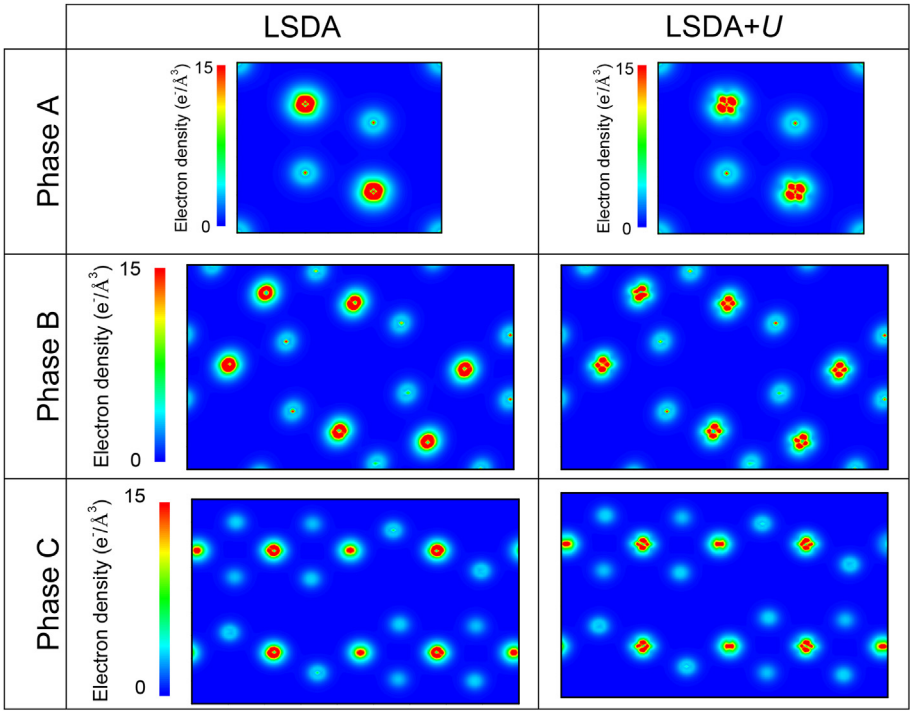

Fig. 6. Electron density plots for Eu_2O_3 over the (110) plane for the A and C phases, and over the (010) plane for the B phase (see text).

In Table 3 we have also included the available experimental values of the EFG at the cationic sites of Gd_2O_3 in the B and C-type phases. These values of V_{zz} where obtained from quadrupole splitting measurements using ^{155}Gd Mössbauer spectroscopy, and considering Q (^{155}Gd) = +1.27 (3)b [54] (see eq. (1)). For the B phase, we took the ΔE_Q values from Ref. [39] and the V_{zz} variation with η as error bar (because the experimental η can not be unambiguously determined with Mössbauer spectroscopy from ΔE_Q). For the C phase we considered the measurements of Ref. [40]. In both cases the experimental data correspond to measurements

Table 3
Predicted values for the principal component V_{zz} (in units of 10^{21} V/m^2) and the asymmetry parameter η of the EFG tensor at each cationic sites of the Ln_2O_3 oxides in the A-, B-, and C-phases. For the A phase, $\eta = 0$ in all cases, as well as in the case of LnC2 site of the C phase.

		A phase	B phase						C phase		
		V_{zz} (Ln)	V_{zz} (Ln1)	η(Ln1)	V_{zz} (Ln2)	η(Ln2)	V_{zz} (Ln3)	η(Ln3)	V_{zz} (LnC1)	η(LnC1)	V_{zz} (LnC2)
Sm_2O_3	LSDA	+14.75	−2.67	0.84	+13.19	0.46	+24.87	0.62	−13.87	0.54	+27.30
	LSDA + U	+12.54	+2.15	0.54	+12.13	0.56	+25.54	0.78	−13.02	0.62	+24.96
Eu_2O_3	LSDA	+15.19	−1.81	0.79	+12.70	0.52	+25.27	0.64	−13.91	0.56	+26.15
	LSDA + U	+14.65	+4.05	0.18	+14.08	0.56	+24.80	0.74	−13.52	0.39	+26.55
Gd_2O_3	LSDA	+15.39	+3.25	0.24	+14.96	0.75	+26.61	0.56	−13.85	0.41	+28.10
	LSDA + U	+15.08	+3.17	0.25	+14.76	0.78	+26.26	0.54	−13.48	0.39	+27.13
	Exp.		2.4 (2) [39]		14 (1) [39]		26 (2) [39]		12.6 (1) [40]		24.6 (1) [40]

performed at low temperatures (12 K or below). As can be seen in Table 3, our first-principles predictions are in excellent agreement with these experimental data.

In the case of the A phase, there is no available measurements of the EFG for Sm_2O_3, Eu_2O_3 or Gd_2O_3. However, we can consider the case of A-La_2O_3 for comparison, which is the only case in which the EFG at the LnA site has been experimentally determined [28,55]. Taking into account our previous analysis, if we consider that the electronic difference between La and Sm, Eu, or Gd atoms should not produce significant changes on the EFG, and that the only difference on it should come from the lanthanide contraction effect, we expect for $|V_{zz}|$ higher values than those reported for A-La_2O_3 (where $V_{zz}^{exp} = 12.32 \times 10^{21}$ V/m^2 at the La site). Our predictions for V_{zz} presented in Table 3 are in good agreement with this assumption. On the other hand, regarding the C phase, there are also measurements of the EFG for other Ln_2O_3 systems (such as Yb_2O_3 and Lu_2O_3, see the compiled list in Ref. [22]). In that case we also found that the current calculations are well framed with the previous studies in that phase.

In order to analyze the origin of the EFG tensor at all the cationic sites, we have to take into account that it is directly related to the electronic density anisotropy in the close vicinity of the Ln nucleus. The major contribution to the EFG at each atomic site comes from the corresponding atomic region, while the lattice term (the contribution originating from the more distant regions of the crystal) is almost negligible (5% or below). Based on this, we will concentrate in the nonspherically valence contributions to V_{zz} by decomposing the EFG according to the different orbital symmetries within the muffin-tin sphere of the corresponding Ln atom. As an example, in Table 4 we present the case of the decomposition of V_{zz} at Gd sites in the three phases of Gd_2O_3 (LSDA calculation). In all cases, the p contribution (V_{zz}^{pp}) clearly dominates over the d and f contributions, while the mixed sd, sp, and pf contributions are negligible. Similar results were found for the LSDA + U calculations, and also in Sm_2O_3 and Eu_2O_3. In all these cases the EFG contribution from p wavefunctions dominates over the d contribution, which can be explained from the fact that the p-orbital first node is closer to the Ln nucleus than that of the d orbital. So, the p-type electronic density is the most anisotropic and hence its contribution to the EFG is the largest one. For Sm_2O_3 and Eu_2O_3, oxides which involve Ln atoms with incomplete 4f shell, the V_{zz}^{ff} contribution is more significant than in Gd_2O_3. This is the reason why in such cases we observed a higher variation of the total V_{zz} when the U term is applied (compared to the Gd_2O_3 case), as already observed in Table 3. The origin of the EFG described above is similar to that previously observed for the EFG at the cationic sites of other Ln_2O_3 systems [22,28].

Table 4
V_{zz} contributions at cationic sites for Gd_2O_3 by LSDA (in units of 10^{21} V/m^2).

	Site	V_{zz}^{pp}	V_{zz}^{dd}	V_{zz}^{ff}	Total V_{zz}
A phase	LnA	+14.80	+0.51	+0.11	+15.39
B phase	LnB1	+3.09	+0.24	+0.01	+3.25
	LnB2	+14.47	+0.52	+0.15	+14.76
	LnB3	+25.75	+1.23	+0.56	+26.26
C phase	LnC1	−13.12	−0.27	−0.67	−13.48
	LnC2	+25.85	+1.29	+0.73	+27.13

Finally, in order to relate the EFG with the cationic local structure we analyzed the V_{zz} directions at Ln sites for the different Ln_2O_3 phases. We present as a representative example the case of Gd_2O_3 in Fig. 7, where the V_{zz} directions are indicated by arrows at each cationic site over the (110) plane for the A and C phases, and over the (010) plane for the B phase. In Fig. 7 we also included the ONN coordination for each cationic site. For the A phase, we found that V_{zz} is oriented along the [0, 0, 1] direction, pointing to the apical O atom, in agreement with the axial symmetry of the LnA site in this phase. In the case of the B phase, for the three LnB sites V_{zz} lies over the ac plane, and tends to be oriented along the [-1,0,1] direction. In this phase, it is not straightforward to correlate the direction of V_{zz} with the local symmetry of each LnB site. Regarding the C phase, the V_{zz} direction depends on the orientation of the Ln octahedral sites. For LnC1, V_{zz} lies over the plane that contains the cation and four ONNs (equatorial plane), while for LnC2 the EFG presents axial symmetry and V_{zz} points out the equatorial plane. We can refine our analysis by considering that LnC1 and LnC2 sites can be described as a Ln atom surrounded by six ONN at the corners of a distorted cube, leaving two corners free: for LnC1 these corners correspond to a cube's face diagonal, while for LnC2 they lie on the cube diagonal. Considering this, we can be more specific and conclude that for LnC1 V_{zz} is orthogonal to that unoccupied face diagonal and lies over a parallel plane to that face, while for LnC2 V_{zz} is oriented along the corresponding cube's free diagonal. These results for the V_{zz} directions in the C phase are practically the same than those obtained with a point charge model in an oversimplified cubic structure [56]. We consider that this agreement with a simpler model is consistent with the ionic nature of the Ln_2O_3 compounds, then the geometry of the structure has a main role on the EFGs.

5. Conclusions

In this work we studied in detail from first principles the structural and electronic properties of the A, B, and C phases of the Ln_2O_3 systems in the middle of the Ln series. We obtained results for the equilibrium structures that fit in the framework of previous APW + lo and PAW predictions for some of the considered compounds [7–10,16,26]. Also, we predicted the pressure-induced phase transformation sequence C→A→B. It is important to remark that previous experimental and *ab initio* studies are not conclusive in what concerns to the phase stability order [1,3,9,13,14,34], hence new experiments could be of great interest in order to solve this controversy.

When we analyze the electronic structure of the equilibrium structures, we found that LSDA predicts a Ln-4f band at E_F, in

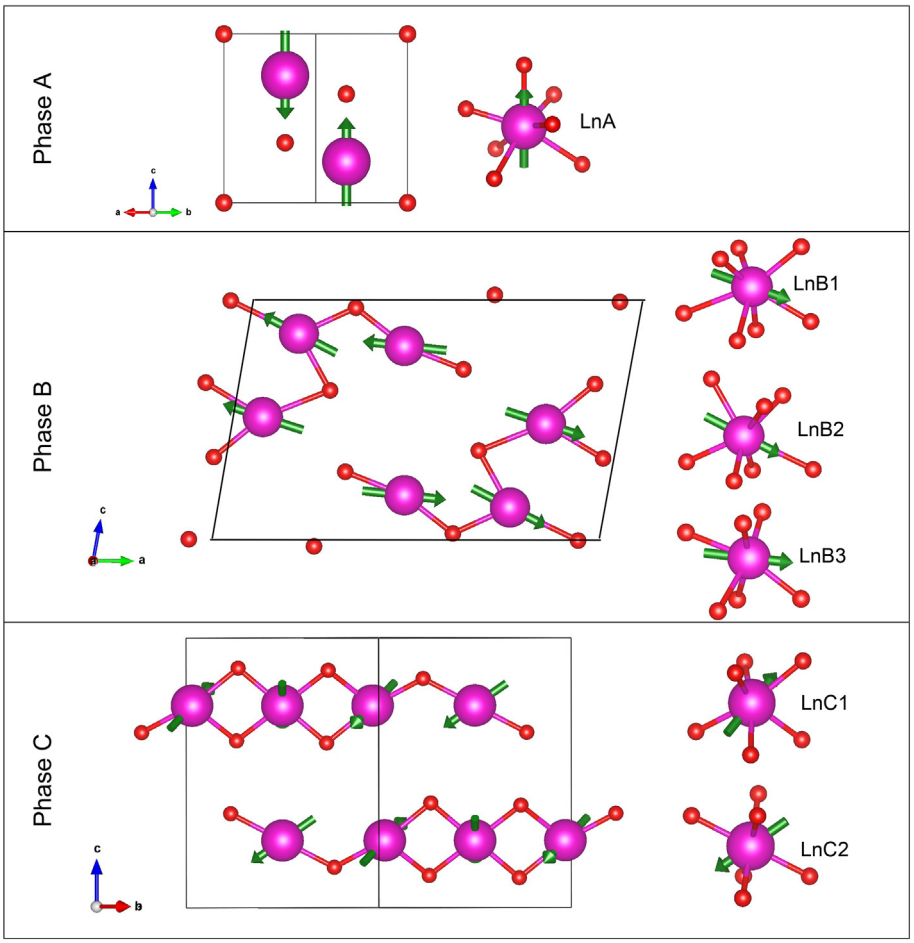

Fig. 7. V_{zz} directions for the cationic sites in A-, B-, and C-phases. In each case, we show a representative atomic layer of the unit cell (which lies over the (110) plane for the A and C phases, and over the (010) plane for the B phase), and the different Ln local structures.

disagreement with the experimental results. The inclusion of the Hubbard term splits this *f* band away from E_F, and the correct insulating ground state of these oxides is predicted. The calculated DOS with LSDA + *U* shows that the CB is composed mainly of Ln-5d states, and a VB with a predominatly O-2*p* character. Our results for the DOS and the projections of the electron density $\rho(\boldsymbol{r})$ are in agreement with the ionic insulator character of these oxides, with a weak covalent bonding between Ln and O atoms.

Regarding the EFG at the cationic sites of these structures, this is the first time an analysis of this tensor is simultaneously performed for the equilibrium structures in the A, B, and C phases of Ln_2O_3 oxides. We analyzed the origin of the EFG at the different Ln sites, and we related it with the local structure. Regarding the EFG origin, we found that the EFG is mostly due to the Ln-*p* orbitals. When we compare our APW + lo calculations with the previous studies of the hyperfine properties on Ln_2O_3 systems, we found that our predicted EFGs are in very good agreement with the experimental data for B- and C-type Gd_2O_3, and with the previous systematics for the A and C phases of Ln_2O_3 oxides [22].

In summary, we obtained an overall good description of the structural and electronic properties for the studied systems by the proposed DFT methods. The inclusion of the Hubbard correction allow an adequate description of the semiconductor character of Ln_2O_3 compounds, without incurring in strong modifications for the predictions of the equilibrium structures and EFGs. This gave us a solid base for the study of emergent properties when these oxides are doped. In particular, we plan performing further investigations for the hyperfine properties in Tantalum doped B-type sesquioxides, which have never been done before, either theoretically nor experimentally.

Acknowledgments

We wish to acknowledge to Consejo Nacional de Investigaciones Científicas y Técnicas (CONICET, under Project Nro. PIP 0803 and PIP 0002) and Universidad Nacional del Noroeste de la Provincia de Buenos Aires (UNNOBASIB Exp. 0176/2017). This research made use of the computational facilities of the Physics of Impurities in Condensed Matter (PhI) group at IFLP and Departamento de Física (UNLP). All authors are members of CONICET, Argentina.

Appendix A. Supplementary data

Supplementary data related to this article can be found at https://doi.org/10.1016/j.cocom.2018.e00327.

References

[1] G. Adachi, N. Imanaka, The binary rare earth oxides, Chem. Rev. 98 (1998) 1479–1514, https://doi.org/10.1021/cr940055h.
[2] M. Zinkevich, Thermodynamics of rare earth sesquioxides, Prog. Mater. Sci. 52 (2007) 597–647, https://doi.org/10.1016/j.pmatsci.2006.09.002.
[3] Y. Zhang, I. Jung, Critical evaluation of thermodynamic properties of rare earth sesquioxides, Calphad 58 (2017) 169–203, https://doi.org/10.1016/j.calphad.2017.07.001.
[4] J.P. McClure, High Pressure Phase Transitions in the Lanthanide Sesquioxides,

PhD Thesis, University of Nevada Las Vegas, USA, 2009.
[5] S.C. Atkinson, Crystal structures and Phase Transitions in the Rare Earth Oxides, PhD Thesis, University of Salford, UK, 2013.
[6] K.A. Irshad, N.V. Chandra Shekar, V. Srihari, K.K. Pandey, S. Kalavathi, High pressure structural phase transitions in Ho:Eu_2O_3, J. Alloy. Comp. 725 (2017) 911–915, https://doi.org/10.1016/j.jallcom.2017.07.224.
[7] N. Hirosaki, S. Ogata, C. Kocer, Ab initio calculation of the crystal structure of the lanthanide Ln_2O_3 sesquioxides, J. Alloy. Comp. 351 (2003) 31–34, https://doi.org/10.1016/S0925-8388(02)01043-5.
[8] L. Petit, A. Svane, Z. Szotek, W.M. Temmerman, First-principles study of rare-earth oxides, Phys. Rev. B 72 (2005), 205118, https://doi.org/10.1103/PhysRevB.72.205118.
[9] B. Wu, M. Zinkevich, F. Aldinger, D. Wen, L. Chen, Ab initio study on structure and phase transition of A- and B-type rare-earth sesquioxides Ln_2O_3 based on density function theory, J. Solid State Chem. 180 (2007) 3280–3287, https://doi.org/10.1016/j.jssc.2007.09.022.
[10] M. Rahm, N.V. Skorodumova, Phase stability of the rare-earth sesquioxides under pressure, Phys. Rev. B 80 (2009), 104105, https://doi.org/10.1103/PhysRevB.80.104105.
[11] H. Jiang, P. Rinke, M. Scheffler, Electronic properties of lanthanide oxides from the GW perspective, Phys. Rev. B 86 (2012), 125115, https://doi.org/10.1103/PhysRevB.86.125115.
[12] Q. Guo, Y. Zhao, C. Jiang, W.L. Mao, Z. Wang, J. Zhang, Y. Wang, Pressure-induced cubic to monoclinic phase transformation in erbium sesquioxide Er_2O_3, Inorg. Chem. 46 (2007) 6164–6169, https://doi.org/10.1021/ic070154g.
[13] Q. Guo, Y. Zhao, C. Jiang, W.L. Mao, Z. Wang, Phase transformation in Sm_2O_3 at high pressure: in situ synchrotron X-ray diffraction study and ab initio DFT calculation, Solid State Commun. 145 (2008) 250–254, https://doi.org/10.1016/j.ssc.2007.11.019.
[14] F.X. Zhang, M. Lang, J.W. Wang, U. Becker, R.C. Ewing, Structural phase transitions of cubic Gd_2O_3 at high pressures, Phys. Rev. B 78 (2008), 064114, https://doi.org/10.1103/PhysRevB.78.064114.
[15] N.V. Skorodumova, R. Ahuja, S.I. Simak, I.A. Abrikosov, B. Johansson, B.I. Lundqvist, Electronic, bonding, and optical properties of CeO_2 and Ce_2O_3 from first principles, Phys. Rev. 64 (2001), 115108, https://doi.org/10.1103/PhysRevB.64.115108.
[16] A.K. Pathak, T. Vazhappilly, Ab initio study on structure, elastic, and mechanical properties of lanthanide sesquioxides, Phys. Status Solidi B (2018), 1700668, https://doi.org/10.1002/pssb.201700668.
[17] M. Topsakal, R.M. Wentzcovitch, Accurate projected augmented wave (PAW) datasets for rare-earth elements, Comput. Mater. Sci. 95 (2014) 263–270, https://doi.org/10.1016/j.commatsci.2014.07.030.
[18] J. Del Plá, R. Pis Diez, Unraveling the apparent dimerization tendency in small Mo_n clusters with n = 3-10, J. Phys. Chem. C 120 (2016) 22750–22755, https://doi.org/10.1021/acs.jpcc.6b07845.
[19] R. Gillen, S.J. Clark, J. Robertson, Nature of the electronic band gap in lanthanide oxides, Phys. Rev. B 87 (2013), 125116, https://doi.org/10.1103/PhysRevB.87.125116.
[20] J.L.F. Da Silva, Stability of the Ce_2O_3 phases: a DFT+ U investigation, Phys. Rev. B 76 (2007), 193108, https://doi.org/10.1103/PhysRevB.76.193108.
[21] M.B. Kanoun, A.H. Reshak, N. Kanoun-Bouayed, S. Goumri-Said, Evidence of Coulomb correction and spin-orbit coupling in rare-earth dioxides CeO_2, PrO_2 and TbO_2: an ab initio study, J. Magn. Magn Mater. 324 (2012) 1397–1405, https://doi.org/10.1016/j.jmmm.2011.11.050.
[22] D. Richard, E.L. Muñoz, M. Rentería, L.A. Errico, A. Svane, N.E. Christensen, Ab initio LSDA and LSDA+U study of pure and Cd-doped cubic lanthanide sesquioxides, Phys. Rev. B 88 (2013), 165206, https://doi.org/10.1103/PhysRevB.88.165206.
[23] B. Huang, Superiority of DFT+U with non-linear core correction for open-shell binary rare-earth metal oxides: a case study of native point defects in cerium oxides, Philos. Mag. A 94 (2014) 3052–3071, https://doi.org/10.1080/14786435.2014.933908.
[24] E.L. Da Silva, A.G. Marinopoulos, R.B.L. Vieira, R.C. Vilão, H.V. Alberto, J.M. Gil, R.L. Lichti, P.W. Mengyan, B.B. Baker, Electronic structure of interstitial hydrogen in lutetium oxide from DFT+U calculations and comparison study with μSR spectroscopy, Phys. Rev. B 94 (2016), 014104, https://doi.org/10.1103/PhysRevB.94.014104.
[25] R.C. Albers, N.E. Christensen, A. Svane, Hubbard-U band-structure methods, J. Phys. Condens. Matter 21 (2009), 343201, https://doi.org/10.1088/0953-8984/21/34/343201.
[26] D. Richard, L.A. Errico, M. Rentería, Structural properties and the pressure-induced C to A phase transition of lanthanide sesquioxides from DFT and DFT+U calculations, J. Alloy. Comp. 664 (2016) 580–589, https://doi.org/10.1016/j.jallcom.2015.12.236.
[27] D. Richard, E.L. Muñoz, T. Butz, L.A. Errico, M. Rentería, Electronic and structural properties, and hyperfine interactions at Sc sites in the semiconductor Sc_2O_3: TDPAC and ab initio study, Phys. Rev. B 82 (2010), 035206, https://doi.org/10.1103/PhysRevB.82.035206.
[28] D. Richard, L.A. Errico, M. Rentería, Electronic, structural, and hyperfine properties of pure and Cd-doped hexagonal La_2O_3 semiconductor, Comput. Mater. Sci. 102 (2015) 119–125, https://doi.org/10.1016/j.commatsci.2015.02.023.
[29] R.W.G. Wyckoff, in: Crystal Structures, vol. 2, Wiley, New York USA, 1964. Chap. 5.
[30] C. Hai-Yong, H. Chun-Yuan, G. Chun-Xiao, Z. Jia-Hua, G. Shi-Yong, L. Hong-Liang, N. Yan-Guang, L. Dong-Mei, K. Shi-Hai, Z. Guang-Tian, Structural transition of Gd_2O_3:Eu induced by high pressure, Chin. Phys. Lett. 24 (2007) 158–160, https://doi.org/10.1088/0256-307X/24/1/043.
[31] D. Lonappan, N.V. Chandra Shekar, P. Ch Sahu, B.V. Kumarasamy, A.K. Bandyopadhyay, M. Rajagopalan, Cubic to hexagonal structural transformation in Gd_2O_3 at high pressure, Phil. Mag. Lett. 88 (2008) 473–479, https://doi.org/10.1080/09500830802232534.
[32] L. Bai, J. Liu, X. Li, S. Jiang, W. Xiao, Y. Li, L. Tang, Y. Zhang, D. Zhang, Pressure-induced phase transformations in cubic Gd_2O_3, J. Appl. Phys. 106 (2009), 073507, https://doi.org/10.1063/1.3236580.
[33] S. Jiang, L. Bai, J. Liu, W. Xiao, X. Li, Y. Li, L. Tang, Y. Zhang, D. Zhang, L. Zheng, The phase transition of Eu_2O_3 under high pressures, Chin. Phys. Lett. 26 (2009), 076101, https://doi.org/10.1088/0256-307X/26/7/076101.
[34] S. Jiang, J. Liu, C. Lin, X. Li, Y. Li, High-pressure x-ray diffraction and Raman spectroscopy of phase transitions in Sm_2O_3, J. Appl. Phys. 113 (2013), 113502, https://doi.org/10.1063/1.4795504.
[35] K.A. Irshad, N.V. Chandra Shekar, Anomalous lattice compressibility of hexagonal Eu_2O_3, Mater. Chem. Phys. 195 (2017) 88–93, https://doi.org/10.1016/j.matchemphys.2017.04.012.
[36] B.J. Kennedy, M. Avdeev, The structure of B-type Sm_2O_3. A powder neutron diffraction study using enriched ^{154}Sm, Solid State Sci. 13 (2011) 1701–1703, https://doi.org/10.1016/j.solidstatesciences.2011.06.020.
[37] G. Chen, J.R. Peterson, K.E. Brister, An energy-dispersive X-ray diffrection study of monoclinic Eu_2O_3 under pressure, J. Solid State Chem. 111 (1994) 437–439, https://doi.org/10.1006/jssc.1994.1250.
[38] N. Dilawar, J. Singh, A. Vijay, K. Samanta, S. Dogra, A.K. Bandyopadhyay, Pressure-induced structural transition trends in nanocrystalline rare-earth sesquioxides: a Raman investigation, J. Phys. Chem. C 120 (2016) 11679–11689, https://doi.org/10.1021/acs.jpcc.6b02104.
[39] J.D. Cashion, D.B. Prowse, A. Vas, Mossbauer effect study of gadolinium compounds using ^{155}Gd, J. Phys. C Solid State Phys. 6 (1973) 2611–2624, https://doi.org/10.1088/0022-3719/6/16/014.
[40] M. Takeda, J. Wang, T. Nichimura, K. Suzuki, T. Kitazawa, M. Takahashi, ^{155}Gd Mössbauer isomer shifts and quadrupole coupling constants of gadolinium complexes, Hyperfine Interact. 156/157 (2004) 359–364, https://doi.org/10.1007/978-1-4020-2852-6_55.
[41] V. Bordovsky, P. Seregin, N. Anisimova, A. Naletko, T. Rabchanova, Mössbauer Study of Rare Earth Metals in Fluoride and Silicate Glasses, Izvestiya of the Russian State Pedagogical University. A.I. Herzen, 2012, pp. 28–37. ISBN 1992-6464.
[42] P. Blaha, K. Schwarz, G. Madsen, D. Kvasnicka, J. Luitz, WIEN2k: an Augmented Plane Wave + Local Orbitals Program for Calculating crystal Properties, Vienna University of Technology, Austria, 2017. ISBN 3-9501031-1-2.
[43] J.P. Perdew, Y. Wang, Accurate and simple analytic representation of the electron-gas correlation energy, Phys. Rev. B 45 (1992), 13244, https://doi.org/10.1103/PhysRevB.45.13244.
[44] V.I. Anisimov, J. Zaanen, O.K. Andersen, Band theory and mott insulators: hubbard U instead of stoner I, Phys. Rev. B 44 (1991) 943, https://doi.org/10.1103/PhysRevB.44.943.
[45] V.I. Anisimov, I.V. Solovyev, M.A. Korotin, M.T. Czyzyk, G.A. Sawatzky, Density-functional theory and NiO photoemission spectra, Phys. Rev. 48 (1993), 16929, https://doi.org/10.1103/PhysRevB.48.16929.
[46] F. Birch, Finite elastic strain of cubic crystals, Phys. Rev. 71 (1947) 809, https://doi.org/10.1103/PhysRev.71.809.
[47] J.S. Weaver, Application of finite strain theory to non-cubic crystals, J. Phys. Chem. Solid. 37 (1976) 711–718, https://doi.org/10.1016/0022-3697(76)90009-3.
[48] P. Blaha, K. Schwarz, P.H. Dederichs, First-principles calculation of the electric-field gradient in hcp metals, Phys. Rev. B 37 (1988) 2792, https://doi.org/10.1103/PhysRevB.37.2792.
[49] P. Haas, F. Tran, P. Blaha, Calculation of the lattice constant of solids with semilocal functionals, Phys. Rev. B 79 (2009), 085104, https://doi.org/10.1103/PhysRevB.79.085104.
[50] J. Xie, S. P. Chen, J. S. Tse, S. de Gironcoli, S. Baroni, High-pressure thermal expansion, bulk modulus, and phonon structure of diamond, Phys. Rev. B 60, 9444. doi: 10.1103/PhysRevB.60.9444.
[51] A. Erba, M. Shahrokhi, R. Moradian, R. Dovesi, On how differently the quasi-harmonic approximation works for two isostructural crystals: thermal properties of periclase and lime, J. Chem. Phys. 142 (2015), 044114, https://doi.org/10.1063/1.4906422.
[52] T. Atou, K. Kusaba, K. Fukuoka, M. Kikuchi, Y. Syono, Shock-induced phase transition of M_2O_3 (M = Sc, Y, Sm, Gd, and In)-type compounds, J. Solid State Chem. 89 (1990) 378, https://doi.org/10.1016/0022-4596(90)90280-B.
[53] A.M. Prokofiev, A.I. Shelykh, B.T. Melekh, Periodicity in the band gap variation of Ln_2X_3 in the lanthanide series, J. Alloy. Comp. 242 (1996) 41–44, https://doi.org/10.1016/0925-8388(96)02293-1.
[54] N.J. Stone, Table of nuclear electric quadrupole moments, Atom Data Nucl Data 111–112 (2016) 1–28, https://doi.org/10.1016/j.adt.2015.12.002.
[55] G.K. Semin, On solving secular equations for half-integer spins in NQR spectroscopy, Russ. J. Phys. Chem. (Engl. Transl.) 81 (2007) 38, https://doi.org/10.1134/S0036024407010104.
[56] A.F. Pasquevich, A.G. Bibiloni, C.P. Massolo, J.A. Vercesi, M. Renteria, K. Freitag, Electric-field gradients at the ^{181}Ta impurity site in Yb, Y, and Dy sesquioxides, Phys. Rev. B 49 (1994), 14331, https://doi.org/10.1103/PhysRevB.49.14331.